Article:
Chen, L., Hassan, H., Tallman, T.N. et al. (2 more authors) (2022) Predicting strain and stress fields in self-sensing nanocomposites using deep learned electrical tomography. Smart Materials and Structures, 31 (4). 045024. ISSN 0964-1726

https://doi.org/10.1088/1361-665x/ac585f

Predicting strain and stress fields in self-sensing nanocomposites using deep learned electrical tomography

Liang Chen[1], Hashim Hassan[2], Tyler N. Tallman[2], Shan-Shan Huang[1] and Danny Smyl[3]

[1] Department of Civil and Structural Engineering, The University of Sheffield, UK
[2] School of Aeronautics and Astronautics, Purdue University, West Lafayette, Indiana
[3] Department of Civil, Coastal, and Environmental Engineering, University of South Alabama, Mobile, Alabama

E-mail: dsmyl@southalabama.edu

Abstract. Conductive nanocomposites, enabled by their piezoresistivity, have emerged as a new instrument in structural health monitoring. To this end, studies have recently found that electrical resistance tomography (ERT), a non-destructive conductivity imaging technique, can be utilized with piezoresistive nanocomposites to detect and localize damage. Furthermore, by incorporating complementary optimization protocols, the mechanical state of the nanocomposites can also be determined. In many cases, however, such approaches may be associated with high computational cost. To address this, we develop deep learned frameworks using neural networks to directly predict strain and stress distributions – thereby bypassing the need to solve the ERT inverse problem or execute an optimization protocol to assess mechanical state. The feasibility of the learned frameworks is validated using simulated and experimental data considering a carbon nanofiber plate in tension. Results show that the learned frameworks are capable of directly and reliably predicting strain and stress distributions based on ERT voltage measurements.

Keywords: Deep learning, electrical resistance tomography, nanocomposites, piezoresistivity

1. Introduction

1.1. Background and context

Composite materials are widely applied in civil, automotive and aerospace industries due to their advanced mechanical properties and applicability for bespoke implementation [1, 2]. Structural health monitoring (SHM) of composite structures is, therefore, a subject of increasing importance, owing to their rising prevalence. In SHM practices, traditional non-destructive testing (NDT) approaches such as magnetic, radiographic, acoustic, ultrasonic and photographic testings have already shown promises in monitoring the structure's conditions [3, 4, 5, 6]. However, locations of (potential) damages are often required as *a priori* for traditional NDT modalities [7], since localized methods are often associated with higher sensitivities in terms of detecting the damage. As a result, their pragmatic applications for a large domains are limited. On the other hand, Electrical Resistance Tomography (ERT) is an imaging modality, which aims at reconstructing conductivity distributions from boundary voltage measurements. It has advantages such as low energy cost, rapid data collection and efficacy to offer spatial monitoring over large areas [8]. To this point, recent studies have shown ERT's benefits for monitoring and evaluation of cement-based materials [9, 10], reconstructing simple and complex crack patterns on concrete elements [11].

In addition to cementitious materials, work has also been done to develop self-sensing polymeric composite materials by incorporating conductive nano-scale phases, such as carbon nanofibers (CNFs) and carbon nanotubes (CNTs). In these materials, electrical transport is a consequence of percolation – electrical current propagates from filler-to-filler through the material. Deformations that alter the connectivity of this network or damage that severs the connection between fillers, therefore, manifest as a conductivity change. Thus, the material is self-sensing via the piezoresistive effect. Unlike traditional point-based sensors, the self-sensing nature of these materials could potentially enable a spatially continuous SHM approach. ERT is, therefore, a natural complement to these materials since it allows for spatially continuous mapping of conductivity changes. The application of ERT to self-sensing polymers has received considerable attention to date [12, 13, 14, 15, 16, 17].

Despite the seemingly high potential of combining self-sensing materials with ERT, some limitations of this approach exist. For example, due to the complexities associated with solving ERT inverse problems, ERT reconstructions often show lower fidelity results compared with some traditional NDT modalities [18]. Efforts have been made to increase the spatial resolution by incorporating prior structural information into the inverse model [11]. Moreover, introducing non-iterative reconstruction methods could reduce the computational time, but at the risk of decreasing the spatial resolution [19]. In addition to these limitations, ERT also does not directly show mechanical effects such as stress or strain. That is, ERT maps electrical conductivity. Even though conductivity is directly dependent on strain in piezoresistive materials, SHM and NDT practitioners would much rather know the strain field directly. To address this limitation, Tallman and colleagues introduced the concept of

piezoresistive inversion [20, 21]. The goal of piezoresistive inversion is to invert the observed conductivity distribution in order to recover the underlying displacement field (and in turn the strain field via kinematic relations and the stress field via elastic constitutive relations). This necessarily requires a suitable macroscale piezoresistivity model that is amenable to general deformations (as opposed to simple uni-axial piezoresistivity models) [22, 23]. Initial work in this area was done using analytical inversion methods [20, 21]; however, it was soon found that these methods can fail to converge to physically meaningful solutions if the strain field is complex. Therefore, metaheuristic methods such as genetic algorithms (GAs), particle swarm optimization, and simulated annealing were next explored [2, 24]. Even though these methods were successful in recovering the strain field from conductivity data, they are limited by their computational expense.

In light of the preceding discussion, we can see that there is considerable potential in truly full-field stress/strain mapping via self-sensing materials + ERT, but existing frameworks for solving this inverse problem have important limitations (i.e. convergence to non-physical solutions and computational cost). We therefore propose to advance the state of the art by applying machine learning techniques to solve this inverse problem with high accuracy and substantially reduced computational cost. The novelty of this work is the development of deep learned frameworks that directly map boundary voltage measurements to the first principal strain and stress distributions via neural networks (NNs) with the aim of achieving continuous and accurate monitoring of self-sensing composites. The proposed frameworks utilize piezoresistive properties of nanocomposites as well as the mapping capabilities of deep learned neural networks to predict the first principal strain and stress fields over the entire domain based on absolute boundary voltage measurements.

1.2. Machine learning and neural networks

Machine learning originated as a research subject in the 1950s for pattern and shape recognition tasks [25, 26]. The concept of perceptrons (Binary classifiers) was initially proposed by Frank Rosenblatt which was later then developed to multi-layer perceptrons (MLP) [26]. With the discovery of back-propagation and the developments of advanced computer infrastructures, machine learning began to draw larger research interest. By increasing the number of perceptrons and layers with expanded training data sets, deep neural networks were later developed and implemented for increasingly complex applications by recognizing non-linear patterns [27, 28]. In initial studies about perceptrons, it was found that a single layer perceptron network was sufficient for recognizing any linear patterns theoretically [29, 30], while the probability of recognizing the desired patterns was directly proportional to the increasing number of perceptrons/neurons [28, 31].

In this paper, we are interested in applying NNs to solve two regression problems aiming to map boundary voltage measurements (V) to the first principal strain and stress spatial distributions (ϵ_p and σ_p), respectively. For this purpose, the mean absolute error (MAE) function with regularization is used as the loss function to train the NNs. The MAE is

formulated as follows:

$$\mathcal{L} = -\frac{1}{N}\sum_{i=1}^{N}|y_i - Y(x_i)| + \lambda||w||^2 \tag{1}$$

In Equation (1), $\mathcal{L}$ represents the loss function which needs to be minimized during the training process. The average of absolute error between i^{th} desired output (y_i) and predicted output ($Y(x_i)$) is calculated across all training samples. N represents the total number of training samples. In addition, an extra L_2 norm is added on all network weights (w) with λ representing the regularization parameter used to avoid over-fitting [32]. In minimizing Equation (1), the proposed NNs are, in essence, generating functions which produce the least error between desired and predicted outputs. Namely, after sufficient training epochs, Y represents the regression mapping from $V \rightarrow \epsilon_p$ or $V \rightarrow \sigma_p$.

Minimization of the loss function is generally achieved by applying a gradient descent algorithm and back-propagation during training [33]. Other machine learning methodologies such as Hopfield Network and Boltzmen Machine based on statistical mechanics can be implemented to minimize the loss function, they are however less applied in pragmatic fields [34, 35]. Principles of applying machine learning in the SHM field are well laid out by Farrar and Worden [7] for the reader's reference. Furthermore, in recent studies, Tibaduiz et al. have shown machine learning can serve as a new damage classification approach [36]. Mousavi et al. has utilized NNs to denoise vibration data for extracting more damage-sensitive features [37]. In this work, since the implementation of the SHM modality often requires big data collection and rapid data processing to achieve continuous monitoring, it is worth remarking that machine learning as a data driven methodology may have great potential when implemented with SHM modalities.

1.3. Paper structure

This paper firstly reviews the historical SHM applications of ERT. Furthermore, this paper discusses the traditional solution to an ERT inverse problem. The experimental data acquisition process for obtaining the absolute voltage measurements on CNF with ERT is introduced in the subsequent section followed by the proposed machine learning methodology. Moreover, we present the formulation of a integrated model (consisting of a elastic mechanical model, complete electrical model and the piezoresistivity model) that is used for generating training data as well as the architectures of the proposed NNs. In the following sections, predictive strain and stress distributions based on simulation and experimental measurements are reported followed by discussions in terms of (a) training data processing, (b) the advantages and disadvantages of the proposed approach and (c) potential future research interests. This paper is then finalized by a conclusion section.

2. Electrical Resistance Tomography

ERT is a diffusive imaging modality which aims to reconstruct the conductivity distribution of a domain from boundary voltage measurements. In the context of ERT data collection, electrodes are installed on the boundary of the domain and then currents are injected into electrodes while potential differences between two electrodes are recorded. Pioneering ERT research was initially developed for medical imaging based on differences between organ conductivities and was then applied on capacities and inductive topographies [38, 39]. During recent research, deep learning methodology have been implemented with ERT in the field of medical imaging. For example, Seo et al. successfully applied a deep learning based method to reconstruct simulated CT scans of lungs [40] and Duan et al. managed to use electrical impedance tomography (EIT) and deep learning to reconstruct real time touch sensing [41]. More recently, engineers and scientists have studied ERT as a SHM and NDT modality. ERT was, in this context, explored to detect damage and visualize strain fields in composite materials [2, 17, 21, 42, 43, 44, 45, 46]. Previous studies have also shown that ERT is a valid modality for detecting crack patterns and reconstructing moisture in cement-based materials [47, 48, 18]. As alluded to previous sections, high fidelity solutions for ERT inverse problems are usually computationally demanding. Therefore, for the aim of achieving condition monitoring systems based on ERT, recent research has implemented machine learning with ERT. For example, Smyl and Liu explored the optimization of electrodes' locations using deep learning to collect more informative measurements [49]. In addition, Hamilton and Hauptmann used deep neural networks to reconstruct ERT images [50]. Chen et al. incorporated NNs to directly reconstruct crack patterns on concrete materials [8]. In addition, researchers explored different deep learning schemes to reconstruct images based on EIT data. For example, Ren et al. utilized a two-stage deep learning method (TSDL) to reconstruct simulated CT scans with high accuracy [51]. Wei et al. used a dominant current deep learning scheme to reconstruct challenging inclusion shapes with a convolutional neural network (CNN) trained with circle or ellipse training data [52]. Furthermore, Wang et al. developed the error-constraint deep learning scheme (Ec-Net) aiming at yielding more robust and accurate reconstruction via mapping the image and error [53]. In the following sections, we introduce the ERT forward model and the conventional solution to ERT inverse problem, followed by the proposed deep learned framework.

2.1. Forward model

In order to solve the ERT inverse problem, a forward model which calculates boundary voltages from conductivity distributions and known measurement/stimulation patterns needs to be formulated alongside physical boundary conditions. Herein, we ultilize the Complete Electrical Model (CEM) developed by Cheng et al. [54] which is written as shown in the following equations:

$$\nabla \cdot (\gamma \nabla u) = 0, x \in \Omega \tag{2}$$

$$\int_{e_l} \gamma \frac{\partial u}{\partial n} dS = I_l, l = 1, ..., L \tag{3}$$

$$\gamma \frac{\partial u}{\partial n} = 0, x \in \partial\Omega \setminus \cup_{l=1}^{L} e_l \tag{4}$$

$$u + z_l \gamma \frac{\partial u}{\partial n} = U_l, l = 1, ..., L. \tag{5}$$

Equation (2) describes steady-state diffusion without internal electricity sources where γ represents the conductivity and u represents the potential distribution within domain Ω. In the CEM, x represents the Cartesian coordinates within Ω. In order to solve Equation (2) and formulate a realistic electrical model, boundary conditions need to be applied as expressed in Equations (3) to (5). I_l represents the injected current on electrodes. Meanwhile, L is the total number of electrodes and e_l represents the l^{th} electrode. In addition, n represents the normal vector on the surface dS on Ω. Equation (5) takes the electrodes' contact impedance into account while calculating the voltage measurement U_l on l^{th} electrode for more accurate modeling. z_l represents the contact impedance between the electrodes and the domain.

$$\sum_{l=1}^{L} I_l = 0 \tag{6}$$

$$\sum_{l=1}^{L} U_l = 0. \tag{7}$$

By enforcing Equations (6) and (7) on the aforementioned equations, we can force the model to obey the current conservation law with fixed potential reference level [17, 55]. The CEM can be discretized for FE analysis. However, in pragmatic (inverse) applications, we are interested in reconstructing the conductivity distributions which are often unknown from boundary voltage measurements. Herein, a unique solution needs to be obtained for an estimation of this ill-posed ERT inverse problem. The traditional solution to an ERT inverse problem is discussed in the following section.

2.2. ERT inverse problem

In this subsection, we discuss the ERT inverse problem to highlight some of the underlying technical aspects of the modality and associated challenges our proposed methodology aims to circumvent. However, before addressing the inverse problem, we would like to emphasize that the ill-posed nature of an ERT inverse problem is mainly resultant from the following

factors: (a) measurement noise from data acquisition, (b) the diffusive nature of electric current, (c) ill-conditioned derivative matrices used in conventional optimization algorithms and (d) numerical modeling errors (e.g. discretization errors in FE implementations). There are two well developed imaging schemes which are absolute and difference imaging. Absolute imaging estimates the conductivity distribution based on voltage measurement from one state. On the other hand, difference imaging estimates the conductivity distribution variation based on voltage measurements from two states. Since we use absolute imaging in this paper, the conventional solution to such scheme is presented in the following paragraph. A typical ERT inverse problem is often first formulated as an observation model by writing

$$V = F(\gamma) \tag{8}$$

where F represents the discretized CEM model. However, due to the existence of measurement and modeling errors, the observation model should be modified as following

$$V = F(\gamma) + e \tag{9}$$

where e represents all potential errors within the inverse problem. The process of solving an ERT inverse problem can then be defined in a least-sqaures (LS) manner

$$\hat{\gamma} = \arg\min\{||V - F(\gamma)||^2\} \tag{10}$$

where $\hat{\gamma}$ represents the conductivity solution. However due to the ill-posed nature of this inverse problem, an unique solution is not guaranteed [56] using conventional LS methods. As an alternative, we can obtain an unique solution ($\hat{\gamma}$) by adding a regularization term to Equation (10) as follows [57]

$$\hat{\gamma} = \arg\min\{||L_e(V - F(\gamma))||^2 + \alpha||L_\gamma\gamma||^2\} \tag{11}$$

where α is a scalar that controls regularization between data fit and smoothness. L_e and L_γ are Cholesky factorized noise weighting and regularization matrices used to weigh uncertainty due to expected measurement noise. Herein, this LS based inverse problem can therefore be solved iteratively by incorporating a Gauss-Newton minimizer formulated as follows

$$\delta\hat{\gamma} = (J^T W J + \alpha L_\gamma^T L_\gamma)^{-1} J^T W (V - F(\gamma)) \tag{12}$$

where $\delta\hat{\gamma}$ is the LS minimizer. The term $J^T W J$ estimates the Hessian matrix while W represents the (non-Cholesky factorized) noise model term. The ill condition of J is, as alluded to earlier, stabilised by the regularization matrix $\alpha L_\gamma^T L_\gamma$. Moreover, studies suggest that by including the noise model term W, we may obtain more accurate solutions by

weighing based on noise level [10]. The above mathematical formulations conclude the traditional solution for an ERT inverse problem in the absolute imaging scheme. Previous research indicates that modeling error can be reduced during the subtraction operation by using difference imaging schemes, hence potentially obtaining more accurate reconstructions [11]. However, in this paper, we adapt the absolute imaging scheme primarily due to the measurement discrepancy between the simulated and experimental data. In order to compensate this modeling error, only absolute imaging data are valid for pre-processing before training. This pre-processing is further discussed in section 5.1. Although we can obtain an accurate estimation of $\hat{\gamma}$ using conventional optimization regimes, computational demands for solving such inverse problem can significantly increase with finer FE meshing and larger domains. Additional computational demands in iterative frameworks include (a) computation of Jacobian matrices and (b) iterative calculations from Newton-based algorithms (e.g. linesearch). Herein, we propose a deep learned framework via NNs to directly predict the first principal strain and stress fields of CNF-based structures without solving the ERT inverse problem using a conventional optimization framework.

3. Experiment Data Acquisition

3.1. CNF specimen and experiment set up

A rectangular CNF-modified epoxy specimen with a nanofiller weight fraction of 1.0% was manufactured for experimental testing. The specimen measured 196 mm $\times$ 46.5 mm with a thickness of 4 mm, and had a central hole of diameter 12.7 mm. Grip tabs were bonded to the specimen using epoxy adhesive to prevent damage due to the gripping pressure of the load frame. The gauge section of the specimen measured 81.1 mm $\times$ 46.5 mm. Electrodes were attached to opposite edges of the gauge section by first painting equally spaced colloidal silver patches and then applying copper tape with extended tabs to the silver patches. Strips of masking tape were applied on top of the copper tape to ensure good contact between the electrodes and the specimen. The fully prepared specimen is shown in Figure 1.

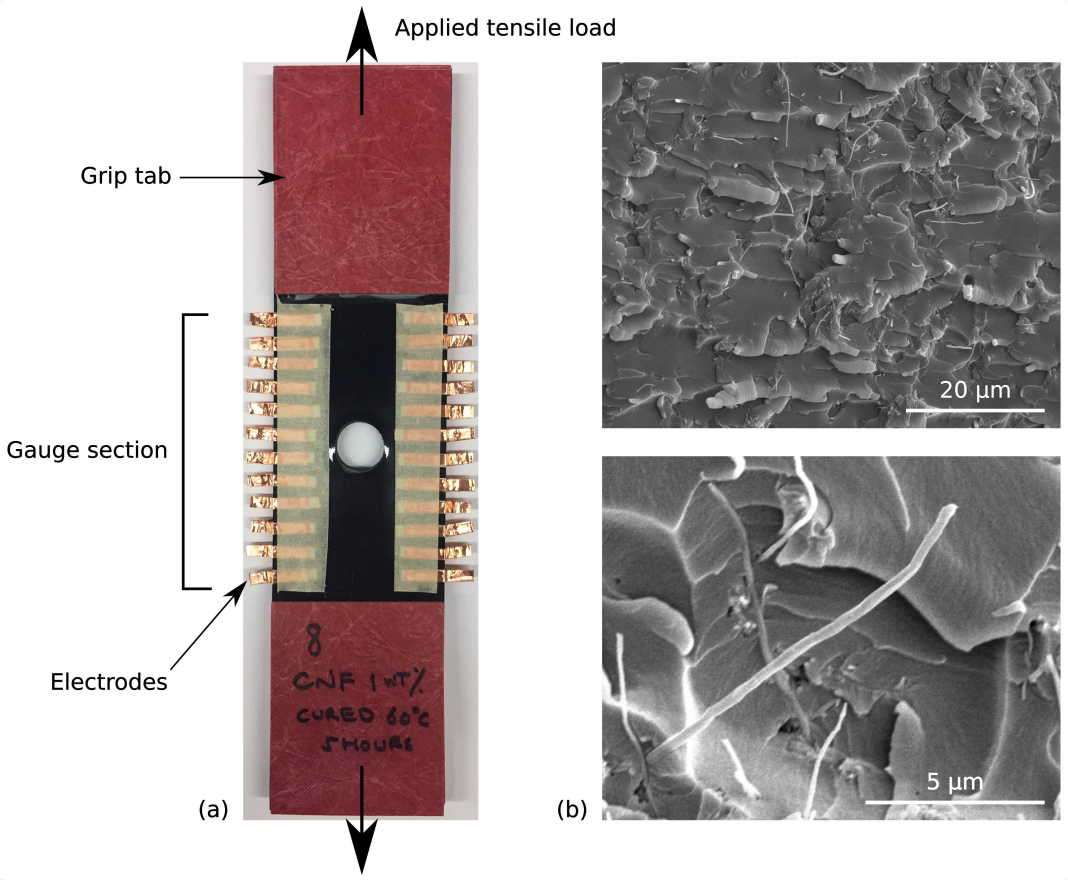

Figure 1. a) Photograph of experimental specimen with electrodes, grip tabs, and gauge section shown. b) SEM images of the underlying CNF network including a close-up of a single CNF.

The specimen was then mounted onto an Instron 8801 load frame and the tabbed portions were fully gripped. The electrodes were connected to a Keithley 6221 current source and a National Instruments PXIe-6368 DAQ to measure the electrode voltages. An 'across' scheme was used for the injections, where current was injected between the first pair of opposing electrodes and voltage differences were measured between the remaining opposing electrode pairs. The current injection was then moved to the next opposing electrode pair and voltage differences between the remaining opposing electrode pairs were again measured. This was repeated until all opposing electrode pairs on the gauge section had received one current injection. This scheme was used to collect one set of voltages from the specimen in its undeformed configuration using a current magnitude of 10 μA. Tensile displacements of $d = 0.25$ mm, 0.50 mm, and 0.75 mm were then applied to the specimen and voltages were collected in each deformed configuration using the same injection scheme and current magnitude.

The specimen was then dismounted from the load frame and the electrode connections were removed. The gauge section was sprayed with white paint and a dotted speckle pattern was applied using a roller dipped in black ink. The specimen was then mounted onto the

load frame again and the tabbed portions were full gripped. A Correlated Solutions digital image correlation (DIC) camera system with a 5 MP resolution was set up and the cameras were focused on the gauge section. DIC data was collected as the specimen was loaded in tension at a constant rate of 1.5 mm/s until failure occurred in the gauge section.

3.2. Piezoresistivity model

As mentioned previously, the piezoresistive inversion process requires a suitable piezoresistivity model. That is, the goal of the inversion process is to find a strain field that, when supplied to the piezoresistivity model, gives rise to the same boundary voltage-current response as observed experimentally. For this, we make use of an analytical piezoresistivity model that was originally developed by Tallman and Wang [22]. In this model, the conductivity of a nanocomposite is predicted by Equation (13) as shown below and based on the model of Takeda et al. [58].

$$\gamma_c = \gamma_m + \frac{4Pv_f l_f}{3\pi\lambda^2 d_f^2 \left(\frac{4l_f}{\pi d_f^2 \gamma_f} + \frac{h^2 t}{Ae^2\sqrt{2m\phi}} \exp \frac{4\pi t}{h}\sqrt{2m\phi}\right)} \tag{13}$$

Above, γ_c is the composite conductivity, γ_m is the matrix conductivity, γ_f is the nanofiller conductivity, P is the percolation probability, v_f is the nanofiller volume fraction, l_f is the nanofiller length, d_f is the nanofiller diameter, λ is the nanofiller waviness ratio, h is Planck's constant, e is the charge of an electron, m is the mass of an electron, ϕ is the potential barrier height felt by a tunneling electron, and t is the average inter-nanofiller separation distance. Conductivity changes are predicted by expressing these model parameters as a function of the infinitesimal strain tensor which is done via excluded volume theory of percolation. Thus, for a given and arbitrary strain state (i.e. given any strain tensor), the new conductivity of the nanocomposite can be predicted. This model was later modified by Tallman and Wang [20] to ensure differentiability.

4. Deep learned ERT tomography framework

4.1. Overview

In this section, we firstly introduce the formulation of deep learned frameworks utilizing NNs followed by providing the rationale of selecting NNs for this investigation. These frameworks aim at directly mapping absolute boundary voltage measurements (V) to first principal strain (ϵ_p) and stress (σ_p) distributions. We select the first principal strain and stress because they are good metrics of material failure for the CNF/epoxy material system. To more clearly distinguish the proposed NN framework from existent genetic algorithm (GA)-based methods of piezoresistive inversion [2], Figure 2 shows the flowchart of determining the mechanical states of the structures via solving the inverse ERT problem and computing GA and figure

3 shows the proposed deep learned framework. The proposed deep learned framework can therefore be succinctly written as

$$N_\epsilon(V) \rightarrow \epsilon_p \tag{14}$$

$$N_\sigma(V) \rightarrow \sigma_p \tag{15}$$

where $N_\epsilon(V)$ and $N_\sigma(V)$ represent the learned NN operators used for predicting ϵ_p and σ_p distributions, respectively. In order to train NNs and learn the embedded mechanical relationships within Equations (14) and (15), an integrated mechanical model needs to be included to generate appropriate training data. This model is introduced in Section 5.1.

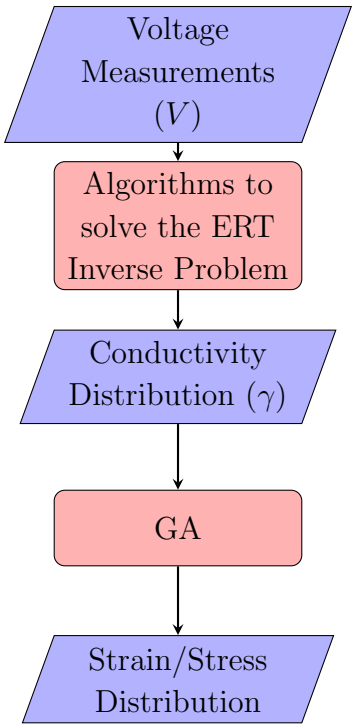

Figure 2. Flowchart of determining the mechanical states via ERT and a GA.

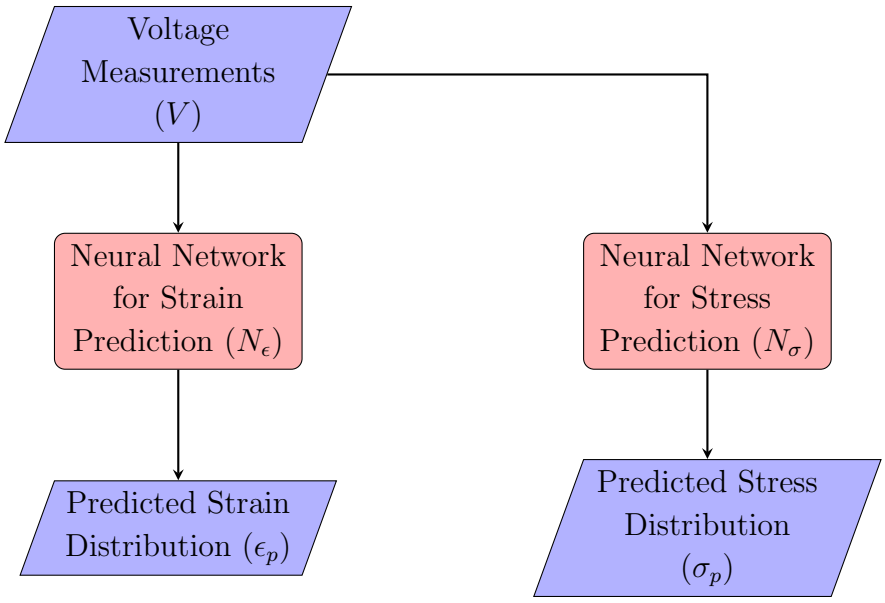

Figure 3. Flowchart of the proposed deep learned framework.

4.2. Selection of regression based machine learning approaches

In this subsection, we discuss the rationale behind the selection of the proposed (NN) framework. In a machine learning context, the pattern recognition tasks in this paper are categorized as regression tasks. There are several approaches which are suitable for regression tasks such as following: (a) linear regression algorithm, (b) logic-based regression models such as boosted decision tree (BRT) regression and random forest (RF) regression, (c) support vector machines (SVMs) and (d) feed-forward artificial neural networks. Linear regression algorithms primarily aim to recognize linear relationships between inputs and outputs based on mean value distributions [59]. However, the patterns in Equations (14) and (15) are highly non-linear, hence linear regression algorithms are inappropriate for this work. In addition, linear regression algorithms have been outperformed by other regression techniques when evaluated on other regression tasks [60, 61]. For logic-based approaches such as BRT and RF, the accuracy of such algorithms has been proven to be affected by the discretization in the input feature [62]. However in our proposed framework, discretization of the voltage measurements might not be the most suitable approach.

Additional studies have shown that SVMs and ANNs can both yield accurate results when being validated against different datasets while SVMs shows more robust performance than ANNs [63, 64]. However, SVM's computational cost increases quadratically with increasing data sizes due to solving quadratic programming problems during training [65]. This drawback remains as a factor inhibiting SVMs from pragmatic applications. Furthermore, implementations can use early stopping, network-reduction and regularization to prevent over-fitting during NNs' training to improve their generalisation performance [32]. Taken the analysis above together, we select NNs for the regression tasks herein, namely for

attaining $N_\epsilon(V)$ and $N_\sigma(V)$ due to their overall accuracy, improved generalisation and large numbers of well-established training tools/toolboxes.

5. Training Data Acquisition and Neural Network Methodology

In this section, we first introduce the integration of the mechanical elastic FE model, CEM and piezoresistivity model used for training data generation. Then, samples of first principal strain and stress distributions used for training are shown. After that, we present the NNs' architectures, training hyper-parameters and the training error curves for both trained NNs.

5.1. Integration of the elastic FE model, CEM and piezoresistivity model

In this work, we aim to recognize the pattern between boundary voltage measurements (V) and first principal strain distributions (ϵ_p) or stress distributions (σ_p) using NNs. For this, we integrated an elastic FE model, CEM and the piezoresistivity model to generate the training data for NNs. The geometry of the domain was adopted from [2]. The elastic FE model discretized the experimental specimen without the top and bottom tabs with reference to Table 1. Figure 5 shows the flowchart of the training data generation. Meanwhile, sample first principal strain and stress distributions for training are shown in Figure 6 and 7. The formulation of the FE model is described as follows:

(i) The geometry of the experimental domain was discretized using 1576 triangular elements and 870 nodes. 24 electrodes were positioned on both vertical sides of the specimen with uniform spacings. The parameters of the domain adopted for discretization are shown in Table 1. Figure 4(a) shows the mesh discretization of the adapted CNF domain where positions of electrodes are highlighted with reference to Table 1.

Table 1. Geometry and mesh details for the adapted CNF specimen domain.

Parameter	Value
Width	46.5 mm
Height	81.1 mm
Electrode spacing	6.2 mm
Electrode width	9.3 mm
Electrode height	3.175 mm
Radius of central notch	6.2 mm

(ii) With FE meshes generated, we adapted CNF material properties from [2] with elastic modulus (E) assigned as 2.534 GPa and Poisson ratio (ν) as 0.35. Furthermore, in order to increase the generalisation performance of NNs for predicting the first principal strain and stress fields on CNF materials, the elastic modulus was distributed randomly within the domain. The homogeneous (mean) value of the elastic modulus was assumed to be 2.534 GPa and the elastic modulus was distributed randomly within the range where

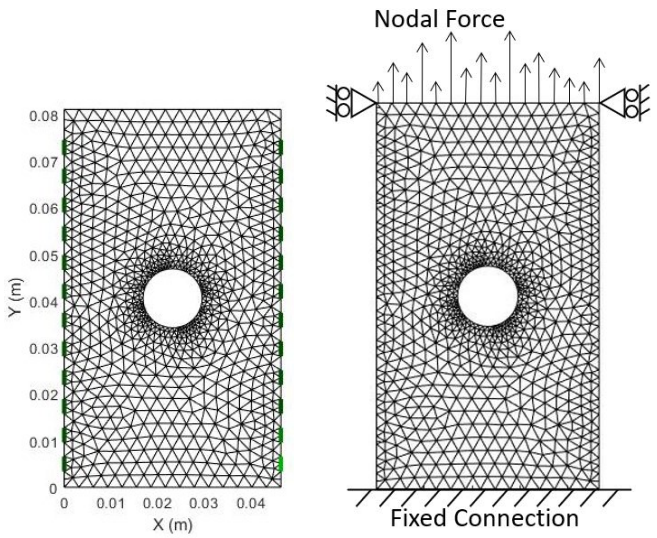

Figure 4. Discretized domain that is used in the integrated model: a) Domain discretization of the gauge section of the CNF/epoxy specimen consisting of 1576 elements and 870 nodes; b) Boundary conditions that are implemented in the elastic FE model. The domain is fixed in x and y directions at the bottom. Displacements are allowed in y-direction on top layer nodes.

$0.6E_h < E < 1.4E_h$. The variance coefficients were selected such that the simulated first principal stress and strain distributions have larger variance while remaining physically realistic. As a result, E data had blob-like Gaussian randomized spatial distributions, which effectively increased the variance of voltage measurements and the corresponding strain/stress distributions within the training sets.

(iii) In the elastic FE model, nodal forces were increased incrementally and randomly on top of the domain. The reasons for doing this are as follows: (a) to simulate the plate under incremental tensile forces corresponding to the experiments and (b) to increase the variance of stress/strain distributions within the training sets. Corresponding boundary condition details are shown in Figure 4(b). Forces were applied on the top nodes acting upwards while constrained in the x-direction. Nodes on the bottom of the mesh were fixed in the x and y directions. The maximum forces used in generating the training data corresponding to the failure displacement in the y-direction adopted from the experiment which was approximately 0.8 mm [2].

(iv) Strain and stress distributions were computed assuming elemental strains and stresses are related using a linear elastic constitutive law. The elemental first principal strains and stresses were then calculated and recorded. After that, the piezoresistivity model developed in [22] and summarized in §3.2 was used to calculate the conductivity distributions (γ) based on strain distributions (ϵ). Finally, the conductivity distributions (γ) were inputted to CEM to compute the corresponding voltage outputs (V).

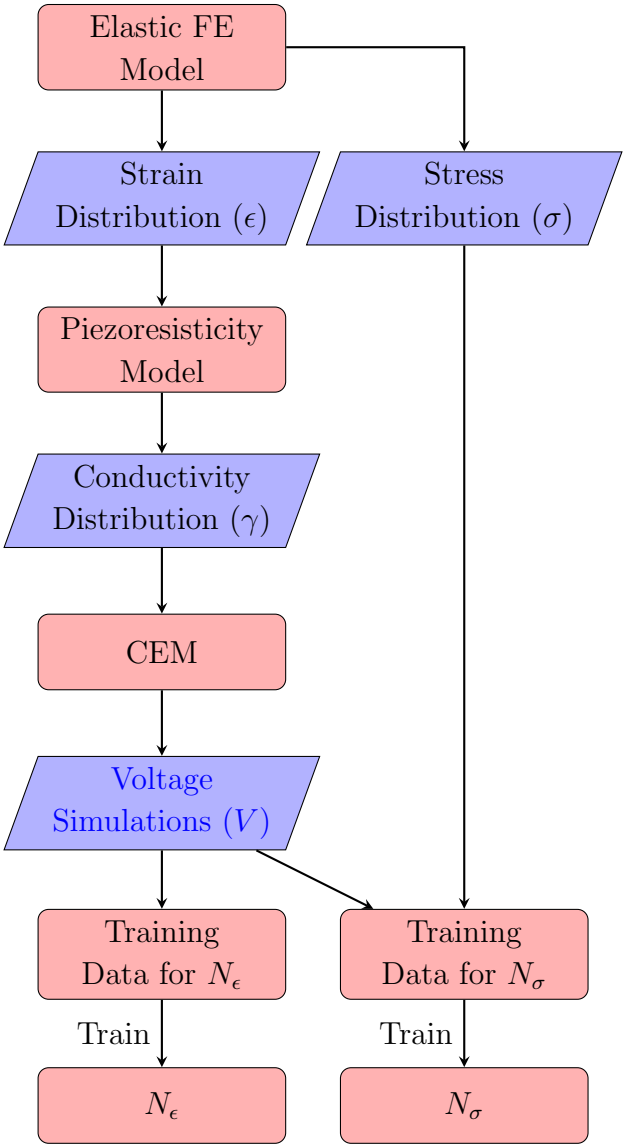

Figure 5. Flowchart of the training data generation path.

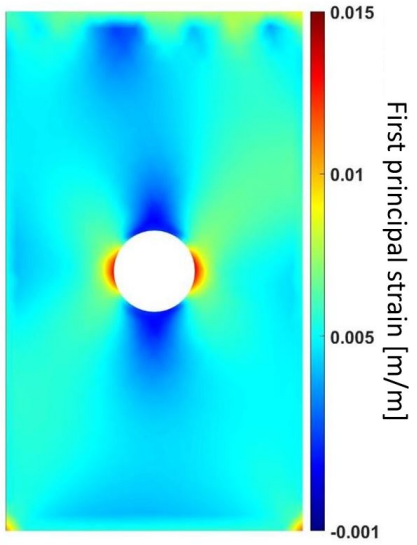

Figure 6. Sample strain distribution within N_ϵ training data.

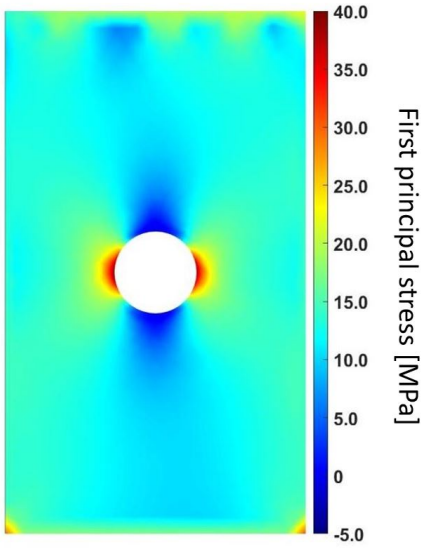

Figure 7. Sample stress distribution within N_σ training data.

5.2. Neural network architecture and training

In this section, we present the NNs' architectures and hyperparameters. From the generation of training data, we obtained two sets of training samples which consist of (a) absolute boundary voltage measurements (V) corresponding to first principal strain distributions (ϵ_p) and (b) absolute boundary voltage measurements (V) corresponding to first principal stress distributions (σ_p). Input data used in training the NNs consist of vectors of size 132×1 while the output data are 1576×1 as shown in Table 2 and 3.

In order to increase the performance of NNs' training (and the accuracy of predictions), the training data was pre-processed prior to training. Namely, in order to reduce the modeling error within the training samples, the following error correction methodology was implemented:

$$e_{model} = V_h - V_0 \tag{16}$$

where e_{model} represents the modeling error, V_h are the CEM voltage simulations from an assumed homogeneous and unstressed sample, and V_0 are the experimental voltage measurements taken from the unstressed reference state. The modeling error was calculated independently as the difference between each index in V_h and V_0, to be more specific, from the first entry to the 132^{th} entry of both these measurement vectors. Homogeneous assignment of the domain's conductivity was made based on prior experimental information where γ_0 is 4.857×10^{-4} S/m. Then, we subtracted e_{model} from voltage simulations in the training data regardless of the forces perturbations to correct and, correspondingly, reduce the modeling error within the samples. As a result, the training samples were better fitted with the experimental measurements.

After correcting model errors, we pre-processed the training samples by eliminating superfluous samples consisting of only zero strain/stress entries. In this way, we can prevent the NNs from being heavily biased towards non-displacement cases. Thirdly, we designed the NNs' architecture and chose the hyper-parameters which yielded the most accurate predictions on the validation sets. Summaries of training sets for N_ϵ and N_σ, number of training samples, architectures and training hyperparameters are shown in Table 2 and 3. The finalized N_ϵ was comprised of one input layer and three fully connected layers with 100 neurons each followed by three dropout layers, respectively. Hyperbolic tangent (Tanh) activation functions were applied on all layers to take advantage of their smooth mapping capabilities. Meanwhile, the finalized N_σ network has the same architecture and activation functions as N_ϵ, however with increased number of neurons to 500 per hidden layer. The reason that N_σ was designed with more neurons than N_ϵ reflects the discrepancy in input to output mapping sizes.

Table 2. Summary of the ANN architecture (N_ϵ) for predicting strain distributions.

Input of V with size (132,1)			
Total number of training samples: 5000			
Layer (Type)	**Activations**	**Learnables Weights**	**Activation Function**
Input layer	132	-	-
Fully connected layer	100	13200	Hyperbolic tangent
Dropout (dropout rate : 50%)	100	-	-
Fully connected hidden layer	100	13200	Hyperbolic tangent
Dropout (dropout rate : 50%)	100	-	-
Fully connected hideen layer	100	13200	Hyperbolic tangent
Dropout (dropout rate : 50%)	100	-	-
Output layer	1576	157600	Hyperbolic tangent
Output of ϵ with size (1576,1)			

Table 3. Summary of the ANN architecture (N_σ) for predicting stress distributions.

Input of V with size (132,1)			
Total number of training samples: 10000			
Layer (Type)	**Activations**	**Learnables Weights**	**Activation Function**
Input layer	132	-	-
Fully connected layer	500	66000	Hyperbolic tangent
Dropout (dropout rate : 50%)	500	-	-
Fully connected hidden layer	500	250000	Hyperbolic tangent
Dropout (dropout rate : 50%)	500	-	-
Fully connected hidden layer	500	250000	Hyperbolic tangent
Dropout (dropout rate : 50%)	500	-	-
Output layer	1576	788000	Hyperbolic tangent
Output of σ with size (1576,1)			

To more comprehensively inform on the training process, training was terminated when the loss function ceased to decrease more than 10% within 500 epochs. The former indicates that gradient descent algorithm has satisfactorily minimized the loss described in Equation (1). This selection was made based on the realization that training after this point may result in over-fitting the data. The minimization of the loss functions for N_ϵ and N_σ are shown in Figures 8 and 9. In these plots, we observe significant loss at the start of the training followed by sharp reduction and finally reached a steady state. In the following section, we will provide results and discussion on predictions made by the trained networks.

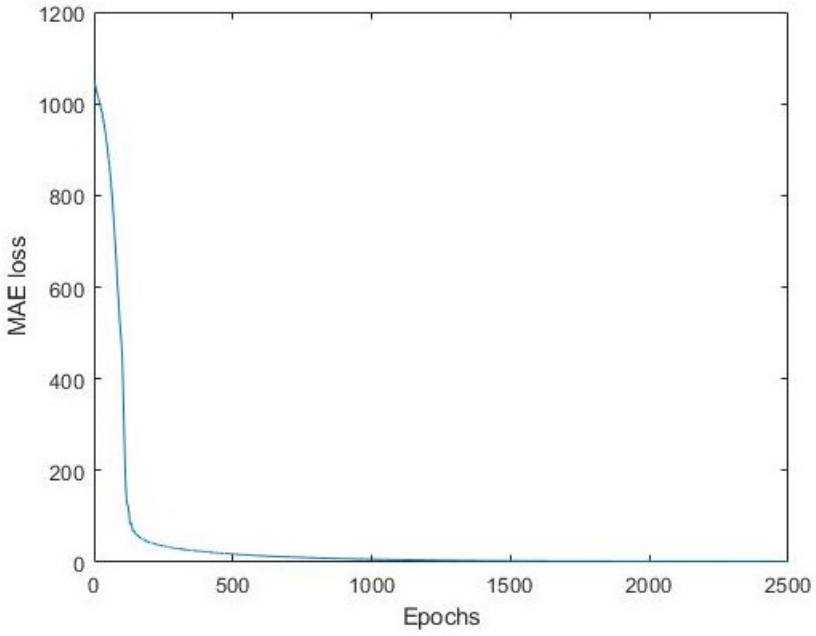

Figure 8. Loss function minimization for the predictor N_ϵ .

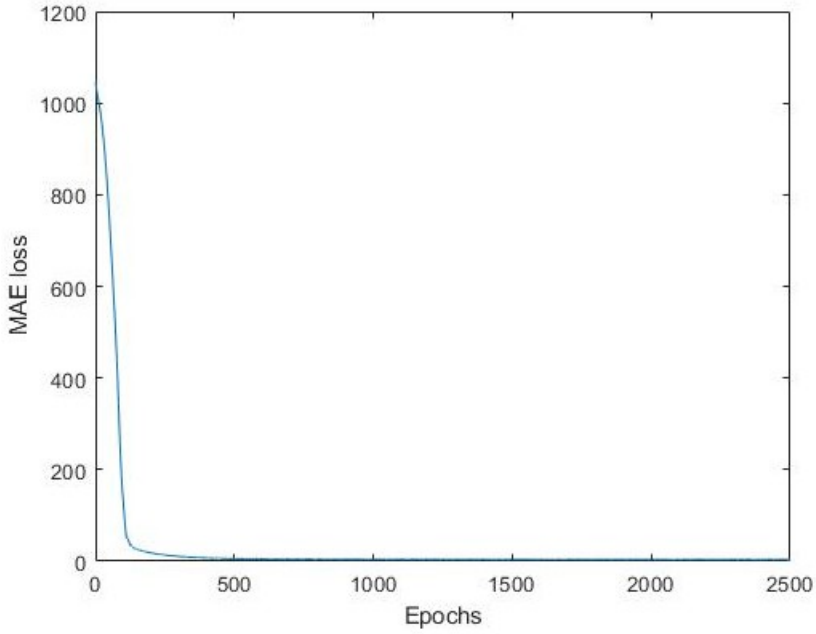

Figure 9. Loss function minimization for the predictor N_σ .

6. Results and Discussion

In this section, we begin by assessing the feasibility of the trained NNs for predicting stress and strain fields. This is first tested using simulated data followed and then with experimental

data. Following, we analyze the results, provide a discussion and lastly consider potential future research.

6.1. Results

The predictive results from N_ϵ and N_σ are shown in Figure 10(a) and (c). The corresponding simulated principal strain and stress distribution are shown in Figure 10(b) and (d). We first observe strain and stress concentrations on top of the domains which are caused by the excess incremental nodal forces during the data generation process. As a whole, the predicted results show similar strain and stress distributions in comparison to the simulated data. However, it can be seen that N_ϵ overpredicts the strain concentration near the circular notch while predictions from N_σ underpredicts the stress concentration on the left-top side of the domain. This can be caused by (a) minimization of the MAE loss function with regularization is highly unlikely to reach zero, hence the prediction error are always present in the results and (b) lower elastic modulus values on nodes due to the random generation of elastic modulus distributions.

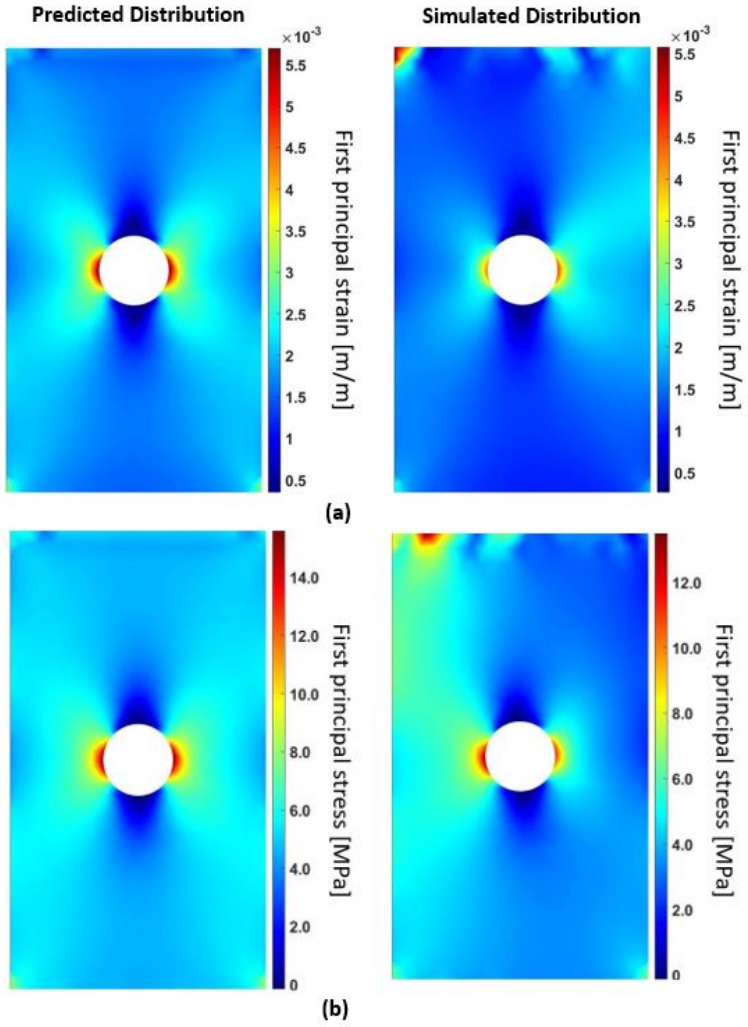

Figure 10. Comparison between the predicted strain and stress distributions and their corresponding simulation samples: a) Prediction of the strain field (left) and simulated strain field from the integrated model (right); b) Prediction of the stress field (left) and simulated stress field from the integrated model (right).

We then validate the NNs predictive performances on the experimental data. The NNs' strain and stress predictions are shown in Figure 11. To corroborate the predictions, Figure 11 also shows the DIC reconstructions from the experiments considering different axial displacements. In this qualitative feasibility study, we observe that the NNs' predictions exhibit similar strain and stress distributions compared with DIC reconstructions. Strain and stress concentrations can also be observed around the notch which are consistent with the DIC results. In addition, it is worth noting that NNs' predictions show correct rate of growth of strain and stress distributions corresponding to different loading stages. Closer inspection of the predictive results show symmetrical first principal strain and stress distribution patterns which are expected based on the applied boundary conditions. Quantitatively speaking, the maximum predictive first principal strain is 17.3% higher than DIC reconstructions

while the maximum predictive first principal stress is 4.5% higher than DIC reconstructions. Discrepancy between the prediction and DIC results can potentially be reduced by optimizing the NNs' hyperparameters. Summarily, in taking the results together, we can observe that the proposed NNs can qualitatively predict the first principal strain and stress distributions directly without solving the ERT inverse problem. Quantitatively speaking, N_σ yields accurate predictions within 5% error margin while N_ϵ outputs less accurate results. The reasons that potentially caused this observation are discussed in the following section.

The computational time for predicting the strain/stress distribution via both methods are recorded in Table 4. We carry out four independent runtime tests via NNs and compare them with the runtimes via $ERT + GA$. Significant computational time reduction can be observed from Table 4. In order to further compare the results of both methodologies. We record the average values of the first principal strain ($\bar{\epsilon}_p$) and stress ($\bar{\sigma}_p$) considering different displacement cases in Table 5. Firstly, results yielded via $ERT + GA$ are down-sampled and mapped on the same FEA meshes that are used for NNs' predictions. Secondly, average values are then computed based on the interpolated strain and stress vectors. The same process is followed when computing the L_2 norm of first principal strain ($\|\epsilon_p\|^2$) and stress vectors ($\|\sigma_p\|^2$) from both methodologies. Corresponding results are recorded in Table 6.

Table 4. Computation runtimes for predicting strain and stress distributions using NNs and ERT + GA considering different displacement cases.

-	**Runtimes via NNs**				**Runtimes via ERT + GA**			
Displacement	**Test** 1	**Test** 2	**Test** 3	**Test** 4	**Test** 1	**Test** 2	**Test** 3	**Test** 4
0.25mm	0.073 s	0.084 s	0.056 s	0.030 s	4440 s	3480 s	3300 s	3300 s
0.50mm	0.029 s	0.028 s	0.031 s	0.029 s	4680 s	3840 s	3600 s	3540 s
0.75mm	0.028 s	0.031 s	0.031 s	0.028 s	4500 s	4200 s	4080 s	4080 s

Table 5. The average first principal strain ($\bar{\epsilon}_p$) and stress distribution ($\bar{\sigma}_p$) obtained via NNs and ERT + GA considering different displacement cases (d).

-	$\bar{\epsilon}_p$ **considering different cases**			$\bar{\sigma}_p$ **considering different cases**		
Methodology	0.25 mm	0.50 mm	0.75 mm	0.25 mm	0.50 mm	0.75 mm
NNs	0.0027	0.0043	0.0064	4.46 MPa	9.24 MPa	14.63 MPa
ERT + GA	0.0061	0.0043	0.0077	15.82 MPa	11.38 MPa	21.39 MPa

Table 6. The L_2 norm of first principal strain ($\|\epsilon_p\|^2$) and stress distribution ($\|\sigma_p\|^2$) obtained via NNs and ERT + GA considering different displacement cases (d).

-	$\|\epsilon_p\|^2$ considering different cases			$\|\sigma_p\|^2$ considering different cases		
Methodology	0.25 mm	0.50 mm	0.75 mm	0.25 mm	0.50 mm	0.75 mm
NNs	0.0848	0.1357	0.2027	144 MPa	297 MPa	470 MPa
ERT + GA	0.2664	0.1314	0.2419	712 MPa	357 MPa	692 MPa

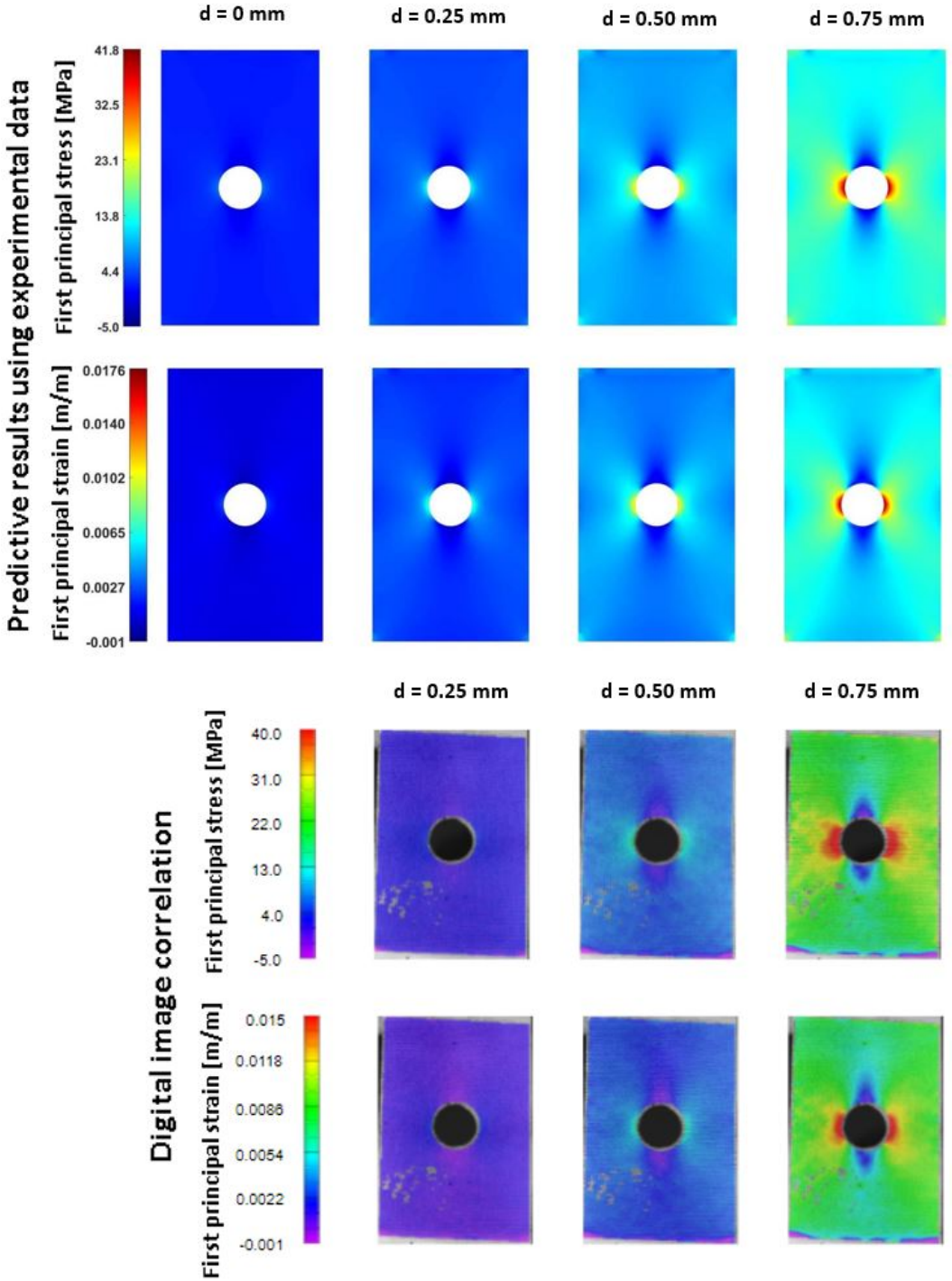

Figure 11. Neural network predictions of experimental data (top two rows) and the DIC reconstructions (bottom two rows) considering different displacement states [2].

6.2. Discussion

This paper conducts the feasibility study of the proposed methodology which is affirmed qualitatively and quantitatively via simulation and experimental data in the preceding sections. Indeed, as corroborated in the previous subsection, we can observe the efficacy of using NNs in directly predicting the first principal strain and stress fields based on ERT voltages measured from CNF materials. The main advantages of the proposed methodology are as follows: (a) reduction in computational costs, having applications in continuous monitoring in pragmatic monitoring frameworks and (b) no prior information such as forces, boundary conditions of the members are required as inputs for NN prediction. Similar features could enable this methodology to be applied in complex environmental and operational conditions. For example, by considering elements that are subjected to varying atmospheric conditions during simulations. To more closely investigate the feasibility of NNs, we will begin by evaluating findings during data processing and network training which improve the accuracy and generalisation of the proposed NNs followed by the insight for future research.

Firstly, we want to address the error correction methodology used to reduce the modeling error prior to training. As shown in Figure 12, we can observe discrepancies between the simulated voltage measurements of homogeneous background estimation and the experimental measurements of the reference state. These discrepancies mainly result from (a) geometrical electrode modeling errors and (b) the elastic FE modeling errors. It is worth noting, regarding (a), that the locations of electrodes are assumed to be stationary regardless of the specimen's elongation. However, in experimental conditions, the locations of electrodes change proportional to the CNF plate displacement. As we can observe from Figure 13, this modeling error correction process mitigates the discrepancies which could increase the accuracy of NNs' predictions when validating experimental results.

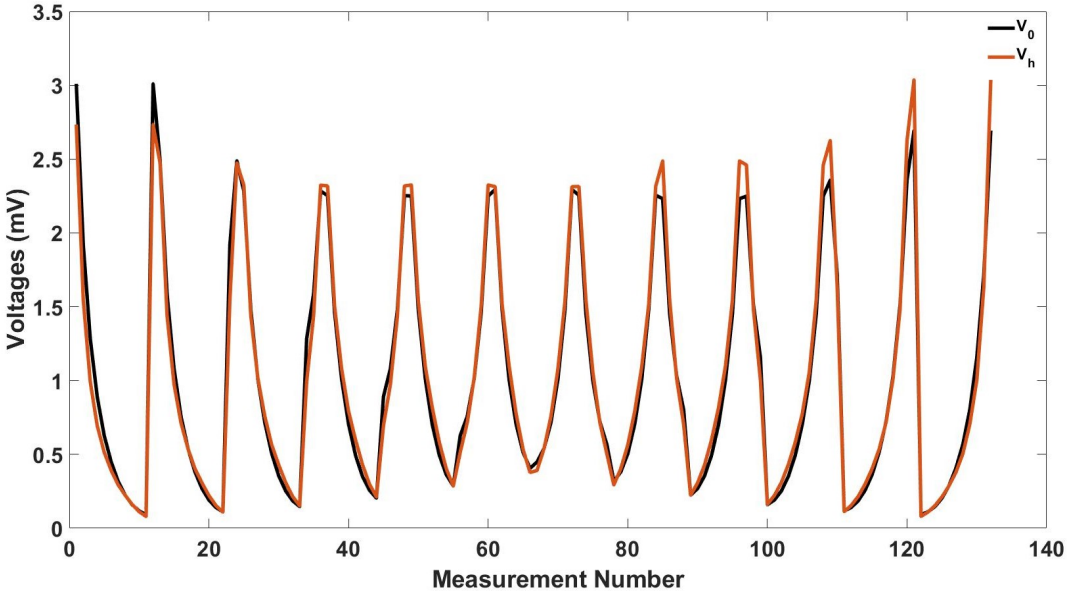

Figure 12. Simulated homogeneous voltages and experimental voltage measurements prior to error correction.

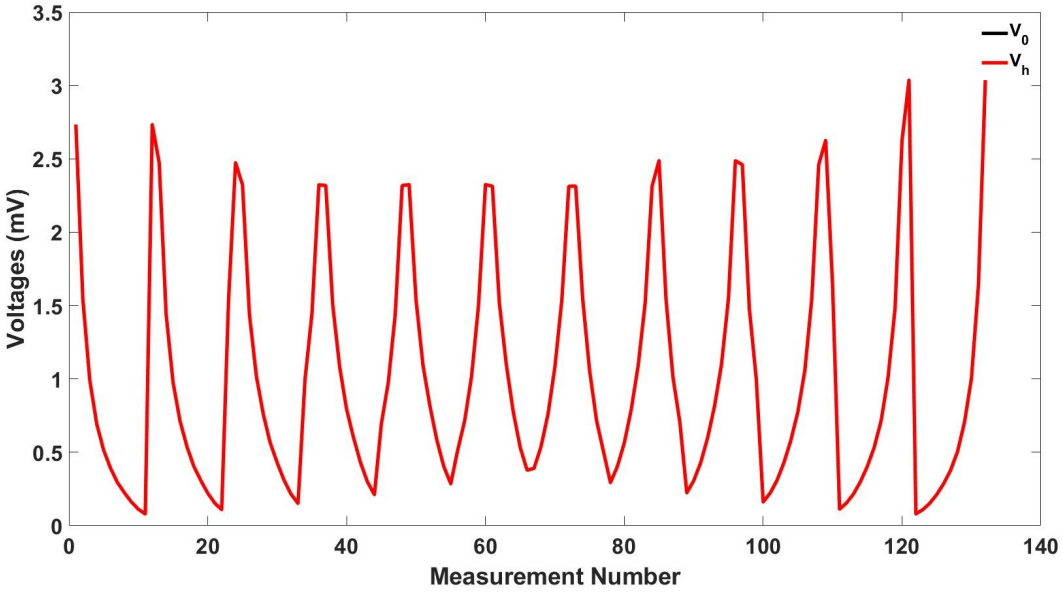

Figure 13. Simulated homogeneous voltages and experimental voltage measurements after error correction.

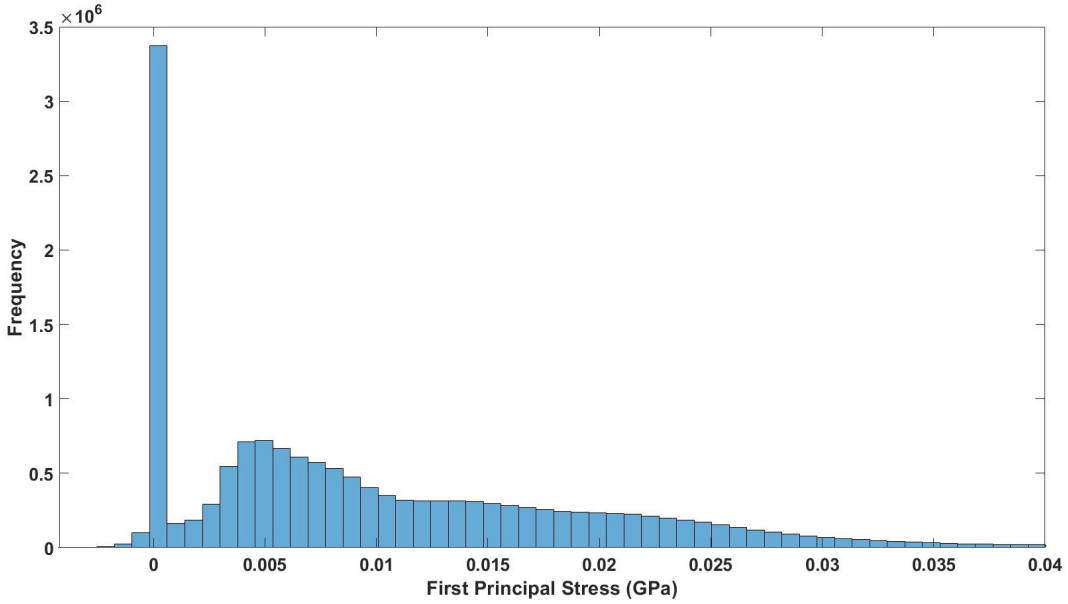

Figure 14. Histogram plot of stress training samples prior to data processing.

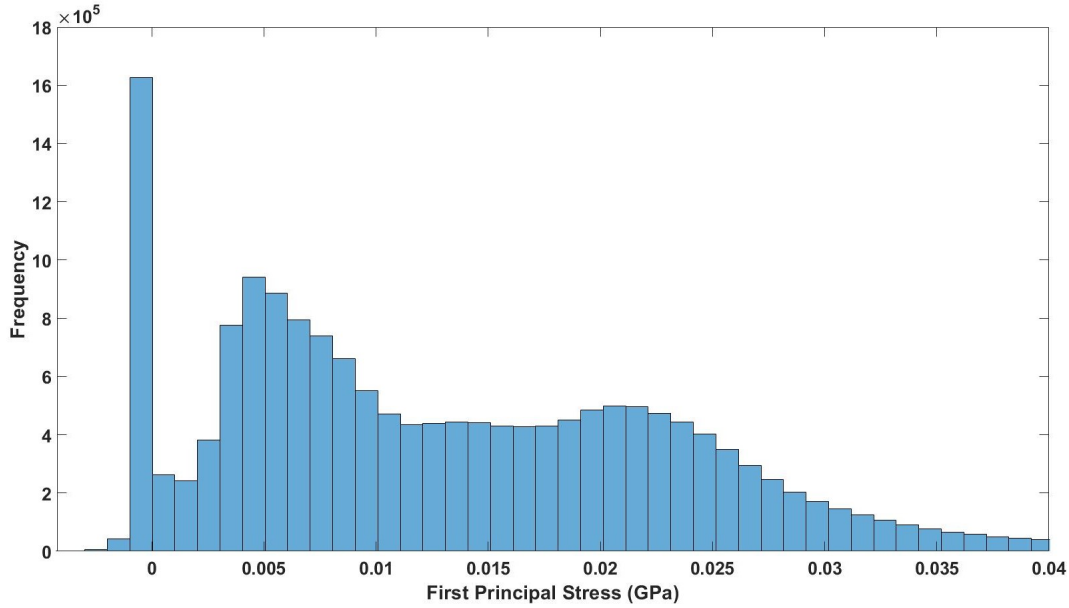

Figure 15. Histogram plot of stress training samples posterior to data processing.

Furthermore, as previously noted, we pre-process the training samples prior to the training process. As shown in Figure 14, training samples are heavily biased towards the 'zero-displacement' cases. This is caused by the generation of training samples originating incrementally from the 'zero-displacement' cases where no or minimal forces are applied on

the model. Hence the entries in strain and stress matrices consist of near-zero entries. Herein, we pre-process the training samples by decreasing the total number of 'zero-displacement' samples with trial and error. Frequency on y-axis represents the number of occurrences of each number within the whole training data set. As a result, Figure 15 shows the histogram plot after processing. Although the spike on zero is still present, we can observe the training samples are now less biased towards 'zero displacement' cases compared to Figure 14. This process proves to be effective during training and yielding more accurate results, however excess elimination of 'zero displacement' samples may result in poor generalization of the NNs.

However, despite the advantages stated above, the performance of NNs is not always satisfactory against certain simulation samples and N_σ yields more accurate results than N_ϵ when validating against experimental data. To explain this, we first note that better performance from N_σ results from the fact that N_σ has more learnable weights than N_ϵ. Though theoretically by increasing the model complexity of N_ϵ, we could obtain a network that yields more accurate predictions, we are at the risk of over-fitting the data. This trade-off between the generalisation and accuracy of the corresponding NNs also caused the errors when predicting on simulated measurements. Hence a rigorous methodology to find the balance point between the generalisation and accuracy for simulated and experimental data at the same time could be a point of potential research interests. The predictive results from simulations show larger error on domain boundaries. This is mainly due to the FEA model used in this paper to generate training samples has high sensitivity to error at top and corner boundary locations as shown in Figure 10. In further research, an efficient posterior error estimation technique can be applied on the FEA model to reduce the error in FEA solutions [66]. As a result, we could have samples with reduced boundary modeling error which could increase the accuracy of predictive results at the boundaries.

To directly compare the computational cost of proposed and reference methodology, we can observe the significant reduction of runtimes of predicting the strain and stress distribution via NNs than $ERT + GA$ in Table 4. This reduction could enable a well-trained neural network to potentially provide real time strain/stress reconstructions under the specific boundary conditions that is trained on. Furthermore, we could observe that NNs yield lower average and L_2 norm values than the $ERT + GA$ methodology as shown in Table 5 and 6. In addition, both average and L_2 norm values shows larger difference when displacement is at 0.25 mm. This could partially be due to the error produces while interpolating the $GA + ERT$ results. We want to address that Table 5 and 6 only provide the direct comparison between two methodologies but not indicate the accuracy of either methods.

In addition, the proposed methodology is application specific. Namely, that the methodology, at present, can only be applied on smart materials which have known piezoresistivity properties since the mapping between conductivity and strain distributions rely on the piezoresistivity model. Herein, potential research can aim at conducting feasibility studies on other smart materials following the proposed methodology. In addition, since the

same boundary conditions are applied on all training samples, NNs in this paper can only yield accurate strain/stress distributions under those specific boundary conditions. In further research, one could either train different NNs based on the expected boundary conditions or adding training samples with different boundary conditions to utilize the advantages of the proposed methodology.

Lastly, since the experimental data were collected in a controlled lab environment, the environmental and operational conditions of this system are assumed to be stable. As a result, the changes in the input data are assumed to be directly associated with the changes of the strain distributions. However, when SHM is applied in field applications, it is imperative for the proposed framework to incorporate any measurement changes caused by the environmental and operational conditions. Hence, future research will be focused on handling robust conditions using advanced data processing approaches (e.g. filtering, cleansing, normalizing, etc.) for measurements used in training stress/strain predictive networks.

7. Conclusion

This paper sets out to assess the feasibility of incorporating neural networks for directly predicting the first principal strain and stress distributions from ERT voltages measured from CNF materials. The findings indicate that the proposed framework can qualitatively predict the principal strain and stress distribution predictions on various experimental voltage measurements. More importantly, the proposed framework may be used to significantly reduce the computational time for the predictions of strain and stress distributions. This advantage may lead to much lower operational costs in pragmatic applications. However, the current study is limited by the absence of approaches to rigorously optimize the trade-off between generalisation and accuracy. Further work needs to be done to research NNs which could yield more quantitatively accurate results on experimental data. In conclusion, the feasibility of proposed framework was affirmed qualitatively with simulation and experimental data. Discussion and future research interests were proposed for further development of the proposed methodology.

8. Acknowledgements

The authors gratefully thank Professor RB Pipes, Dr. Benjamin Denos and Dr. Rebecca Cutting for their assistance with DIC performed at the Composites Manufacturing and Simulation Center at Purdue University. Dr. Christopher Gilpin in the Purdue Electron Microscopy Facility is also thanked for performing the SEM imaging. Thanks to Adrien Gallet for insightful discussions on this paper.

References

[1] Mangalgiri P 1999 *Bulletin of Materials Science* **22** 657–664
[2] Hassan H and Tallman T N 2020 *Structural Health Monitoring* **19** 765–780
[3] Gholizadeh S 2016 *Procedia Structural Integrity* **1** 50–57
[4] Mutlib N K, Baharom S B, El-Shafie A and Nuawi M Z 2016 *Structural Control and Health Monitoring* **23** 409–422
[5] Montinaro N, Cerniglia D and Pitarresi G 2018 *NDT & E International* **98** 134–146
[6] Kong X and Li J 2018 *Computer-Aided Civil and Infrastructure Engineering* **33** 783–799
[7] Farrar C R and Worden K 2012 *Structural health monitoring: a machine learning perspective* (John Wiley & Sons)
[8] Chen L, Gallet A, Huang S S, Liu D and Smyl D 0 *Structural Health Monitoring* **0** 14759217211037236
[9] Karhunen K, Seppänen A, Lehikoinen A, Monteiro P J and Kaipio J P 2010 *Cement and Concrete Research* **40** 137–145
[10] Smyl D 2020 *Construction and Building Materials* **244** 118299
[11] Smyl D, Pour-Ghaz M and Seppänen A 2018 *NDT & E International* **99** 123–133
[12] Tallman T N, Gungor S, Wang K and Bakis C E 2015 *Structural Health Monitoring* **14** 100–109
[13] Thomas A, Kim J, Tallman T and Bakis C 2019 *Composites Part B: Engineering* **177** 107276
[14] Gallo G J and Thostenson E T 2016 *Composite Structures* **141** 14–23
[15] Gallo G J and Thostenson E T 2015 *Materials today communications* **3** 17–26
[16] Baltopoulos A, Polydorides N, Pambaguian L, Vavouliotis A and Kostopoulos V 2015 *Composites Part B: Engineering* **76** 149–158
[17] Tallman T N and Smyl D J 2020 *Smart Materials and Structures* **29** 123001
[18] Smyl D, Bossuyt S, Ahmad W, Vavilov A and Liu D 2020 *Structural Health Monitoring* **19** 215–239
[19] Ferreira A and Novotny A 2017 *Inverse Problems* **33** 035005
[20] Tallman T and Wang K 2016 *Smart Materials and Structures* **25** 115046
[21] Tallman T, Gungor S, Koo G and Bakis C 2017 *Journal of Intelligent Material Systems and Structures* **28** 2617–2629
[22] Tallman T and Wang K 2013 *Applied Physics Letters* **102** 011909
[23] Koo G and Tallman T 2020 *Composites Part B: Engineering* **190** 107907
[24] Hassan H and Tallman T N 2020 *IEEE Sensors Journal* **21** 659–666
[25] Kröse B, Krose B, van der Smagt P and Smagt P 1993
[26] Rosenblatt F 1958 *Psychological review* **65** 386
[27] Goodfellow I, Bengio Y, Courville A and Bengio Y 2016 *Deep learning* vol 1 (MIT press Cambridge)
[28] LeCun Y, Bengio Y and Hinton G 2015 *nature* **521** 436–444
[29] Papert S 1961 Some mathematical models of learning *Proceedings of the fourth London symposium on information theory*
[30] Baum E B 1988 *Journal of complexity* **4** 193–215
[31] Bishop C M *et al.* 1995 *Neural networks for pattern recognition* (Oxford university press)
[32] Ying X 2019 An overview of overfitting and its solutions *Journal of Physics: Conference Series* vol 1168 (IOP Publishing) p 022022
[33] LeCun Y, Boser B, Denker J S, Henderson D, Howard R E, Hubbard W and Jackel L D 1989 *Neural computation* **1** 541–551
[34] Hopfield J J 1982 *Proceedings of the national academy of sciences* **79** 2554–2558
[35] Ackley D H, Hinton G E and Sejnowski T J 1985 *Cognitive science* **9** 147–169
[36] Tibaduiza D, Torres-Arredondo M Á, Vitola J, Anaya M and Pozo F 2018 *Complexity* **2018**
[37] Mousavi Z, Varahram S, Ettefagh M M, Sadeghi M H and Razavi S N 2020 *Structural Health Monitoring* 1475921720932614
[38] Henderson R P and Webster J G 1978 *IEEE transactions on bio-medical engineering* **25** 250–4
[39] Yang W and York T 1999 *IEE Proceedings-Science, Measurement and Technology* **146** 47–53

[40] Seo J K, Kim K C, Jargal A, Lee K and Harrach B 2019 *SIAM journal on Imaging Sciences* **12** 1275–1295
[41] Duan X, Taurand S and Soleimani M 2019 *Scientific reports* **9** 1–11
[42] Loh K J, Kim J, Lynch J P, Kam N W S and Kotov N A 2007 *Smart Materials and Structures* **16** 429
[43] Loh K J, Hou T C, Lynch J P and Kotov N A 2009 *Journal of nondestructive evaluation* **28** 9–25
[44] Loyola B R, Briggs T M, Arronche L, Loh K J, La Saponara V, O'Bryan G and Skinner J L 2013 *Structural Health Monitoring* **12** 225–239
[45] Lestari W, Pinto B, La Saponara V, Yasui J and Loh K J 2016 *Smart Materials and Structures* **25** 085016
[46] Tallman T, Gungor S, Wang K and Bakis C 2014 *Smart Materials and Structures* **23** 045034
[47] Smyl D and Liu D 2019 *IEEE Sensors Letters* **3** 1–4
[48] Hallaji M, Seppänen A and Pour-Ghaz M 2015 *Cement and Concrete Research* **69** 10–18
[49] Smyl D and Liu D 2020 *IEEE Transactions on Instrumentation and Measurement* **69** 6030–6044
[50] Hamilton S J and Hauptmann A 2018 *IEEE transactions on medical imaging* **37** 2367–2377
[51] Ren S, Sun K, Tan C and Dong F 2019 *IEEE Transactions on Instrumentation and Measurement* **69** 4887–4897
[52] Wei Z, Liu D and Chen X 2019 *IEEE Transactions on Biomedical Engineering* **66** 2546–2555
[53] Wang Q, Zhang H, Li X, Duan X, Wang J, Zhang R, Zhang H, Ma Y, Wang H and Jia J 2021 *IEEE Transactions on Instrumentation and Measurement*
[54] Cheng K S, Isaacson D, Newell J and Gisser D G 1989 *IEEE Transactions on Biomedical Engineering* **36** 918–924
[55] Vauhkonen M, Vadasz D, Karjalainen P A, Somersalo E and Kaipio J P 1998 *IEEE transactions on medical imaging* **17** 285–293
[56] Sarvas J 1987 *Physics in Medicine & Biology* **32** 11
[57] Smyl D, Hallaji M, Seppänen A and Pour-Ghaz M 2016 *International Journal of Heat and Mass Transfer* **103** 1348–1358
[58] Takeda T, Shindo Y, Kuronuma Y and Narita F 2011 *Polymer* **52** 3852–3856
[59] Maulud D and Abdulazeez A M 2020 *Journal of Applied Science and Technology Trends* **1** 140–147
[60] Baharvand S, Jozaghi A, Fatahi-Alkouhi R, Karimzadeh S, Nasiri R and Lashkar-Ara B 2020 *Iranian Journal of Science and Technology, Transactions of Civil Engineering* 1–14
[61] Smoliński S and Radtke K 2017 *ICES Journal of Marine Science* **74** 102–111
[62] An A and Cercone N 1999 Discretization of continuous attributes for learning classification rules *Pacific-Asia Conference on Knowledge Discovery and Data Mining* (Springer) pp 509–514
[63] Niu W J, Feng Z K, Feng B F, Min Y W, Cheng C T and Zhou J Z 2019 *Water* **11** 88
[64] Shirzad A, Tabesh M and Farmani R 2014 *KSCE Journal of Civil Engineering* **18** 941–948
[65] Ertekin S and Hopper G 2006 Efficient support vector learning for large datasets *Grace Hopper Celebration of Women in Computing* (Citeseer)
[66] Ainsworth M and Oden J T 1997 *Computer methods in applied mechanics and engineering* **142** 1–88